

Numerical study of the two-boson bound-state problem with and without partial-wave decomposition

Wolfgang Schadow*

*Caribou3D Research & Development
53424 Remagen, Kirchplatz 1, Germany*

(Dated: January 21, 2026)

The validation of numerical methods is a prerequisite for reliable few-body calculations, particularly when moving beyond standard partial-wave decompositions. In this work, we present a precision benchmark for the two-boson bound-state problem, solving it using two complementary formulations: the standard one-dimensional partial-wave Lippmann–Schwinger equation and a two-dimensional formulation based directly on vector variables. While the partial-wave approach is computationally efficient for low-energy bound states, the vector-variable formulation becomes essential for scattering applications at higher energies where the partial-wave expansion converges slowly. We demonstrate the high-precision numerical equivalence of both methods using rank-one separable Yamaguchi potentials and non-separable Malfliet–Tjon interactions. Furthermore, for the Yamaguchi potential, we derive exact analytical expressions quantifying the systematic errors introduced by finite momentum- and coordinate-space cut-offs. These analytical bounds provide a rigorous tool for disentangling discretization errors from truncation effects in few-body codes. The results establish a reliable reference standard for validating the vector-variable approaches essential for future three- and four-body calculations.

PACS numbers: 21.45.-v, 03.65.Ge, 02.60.Nm, 03.65.Nk

Keywords: Two-body bound state, Lippmann–Schwinger equation, Momentum space, Vector variables, Partial-wave decomposition, Yamaguchi potential, Malfliet–Tjon potential, Numerical benchmarks

I. INTRODUCTION

The description of systems of three or more interacting particles, as encountered in atomic and nuclear physics, requires the solution of the Faddeev or Faddeev–Yakubovsky equations [1–13]. Their numerical implementation is a computationally demanding task, for which reliable verification and precise error control are essential. A well-established strategy for validating such calculations is their application to simpler subsystems for which high-precision or analytical results are available.

The two-boson bound-state problem serves as an ideal benchmark in this context. Although it represents the simplest bound-state system, it already contains key features of the interaction and the underlying quantum mechanics. The binding energy and wave function can therefore be used to test numerical accuracy, quadrature schemes, and the treatment of singular behavior in a controlled setting.

While the partial-wave decomposition (PWD) is the standard method for solving the Schrödinger equation at low energies, it becomes computationally burdensome in scattering calculations at intermediate and high energies due to the slow convergence of the partial-wave series. In such regimes, formulations based directly on vector variables, which avoid the angular momentum expansion, are advantageous [1–3, 10]. However, these vector-variable formulations lead to higher-dimensional integral equations that require careful numerical handling of singularities and interpolations. Before applying these methods to complex

three- and four-body calculations, it is imperative to validate the numerical framework against a system where the PWD result is exact and numerically cheap. The two-boson bound state serves as this rigorous test bed.

In this work, we construct such a benchmark by solving the Lippmann–Schwinger equation for the two-boson ground state in two complementary ways. The first is the conventional approach based on a partial-wave decomposition, which leads to a set of uncoupled one-dimensional integral equations. The second avoids a partial-wave expansion and treats the equation directly as a two-dimensional integral equation in momentum magnitude and angle between the momenta. This formulation is closer to the structure encountered in three-body calculations and allows for a direct comparison of numerical performance.

To demonstrate the robustness of the methods, we consider two classes of interactions. The rank-one separable Yamaguchi potential [14, 15] allows analytical solutions and enables a direct comparison with exact results. In addition, it permits the derivation of closed expressions for the systematic errors introduced by momentum- and coordinate-space cut-offs. As a more realistic example, we study local Malfliet–Tjon potentials [16], which are of Yukawa type [17] and pose different numerical challenges due to their short-range structure. The two-body equations cannot be solved in simple closed form; only approximate methods [18, 19] or analytical expansions based on supersymmetry [20] are available.

This paper is organized as follows. In Sec. II, we derive the partial-wave-projected Lippmann–Schwinger equation for the two-boson bound state. Section III presents the corresponding two-dimensional formulation. The applications to the Yamaguchi and Malfliet–Tjon potentials are

* wolfgang.schadow@caribou3d.com

discussed in Secs. IV and V. The numerical methods are described in Sec. VI. Results and convergence studies are presented in Sec. VII. Section VIII summarizes the work. The appendices collect analytical expressions for expectation values of the Yamaguchi potential in momentum and coordinate space.

The specific contributions of this work beyond previous studies include the derivation of exact analytical expressions for the systematic errors induced by finite momentum- and coordinate-space cut-offs for the Yamaguchi potential, and a precision benchmark of the vector-variable formulation achieving 10^{-10} MeV consistency with partial-wave results, validating the method for future high-precision applications.

II. PARTIAL-WAVE-PROJECTED LIPPMANN–SCHWINGER EQUATION

We consider the two-boson bound-state problem in momentum space and set $\hbar = c = 1$. The mass of each boson is chosen as $m_N = 1$, which implies a reduced mass $\mu = 1/2$. The binding energy E and the bound-state wave function $|\psi\rangle$ are determined from the Schrödinger equation

$$H|\psi\rangle = (H_0 + V)|\psi\rangle = E|\psi\rangle, \quad (1)$$

where we work in the two-body center-of-mass frame. The free Hamiltonian is given by $H_0 = p^2$, and V denotes the two-body interaction. Note that with these definitions, the energy E has dimensions of inverse length squared (fm $^{-2}$). Physical energies in MeV are obtained by multiplication with the conversion factor $(\hbar c)^2/m_N$.

Equation (1) can be written in Lippmann–Schwinger form as

$$|\psi\rangle = \frac{1}{E - H_0} V |\psi\rangle. \quad (2)$$

For bound states, the energy is negative. Throughout this work, we denote the two-body binding energy as $E_2 < 0$. For the Yamaguchi potential, we specifically write $E_2 = -\alpha^2$. Since $E_2 < 0$, the denominator $E_2 - p^2$ in the integral equation does not vanish for any real momentum $p \geq 0$.

To solve this equation, we project onto momentum states and introduce partial-wave states $|plm\rangle$. These states satisfy the completeness relation

$$1 = \sum_{lm} \int_0^\infty dp p^2 |plm\rangle \langle plm|, \quad (3)$$

and are normalized according to

$$\langle plm|p'l'm'\rangle = \delta_{ll'} \delta_{mm'} \frac{\delta(p - p')}{p^2}. \quad (4)$$

Here, p denotes the relative momentum, l the orbital angular momentum, and m the corresponding magnetic quantum number.

After projection with $\langle plm|$ and insertion of the completeness relation (3), Eq. (2) becomes

$$\begin{aligned} \psi_{lm}(p) \equiv \langle plm|\psi\rangle &= \sum_{l'm'} \int_0^\infty dp' p'^2 \frac{1}{E - p'^2} \\ &\times \langle plm|V|p'l'm'\rangle \psi_{l'm'}(p'). \end{aligned} \quad (5)$$

We restrict our study to spherically symmetric interactions without tensor forces. In this case, the matrix element of the potential is diagonal in the angular momentum quantum numbers,

$$\langle plm|V|p'l'm'\rangle = \delta_{ll'} \delta_{mm'} V_l(p, p'), \quad (6)$$

with the partial-wave-decomposed potential given by

$$V_l(p, p') = \int_{-1}^1 d(\cos \theta) P_l(\cos \theta) V(\mathbf{p}, \mathbf{p}'). \quad (7)$$

Here, θ denotes the angle between the relative momentum vectors \mathbf{p} and \mathbf{p}' . As a result, Eq. (5) reduces to

$$\psi_l(p) = \int_0^\infty dp' p'^2 \frac{1}{E - p'^2} V_l(p, p') \psi_l(p'), \quad (8)$$

which is the one-dimensional Lippmann–Schwinger equation. Since the equation is independent of m , the magnetic quantum number has been omitted.

For the interactions considered here, only the $l = 0$ partial wave supports a bound state. We therefore restrict the discussion to this channel and drop the angular momentum indices for the wave function. The wave function is normalized according to

$$1 = \langle \psi | \psi \rangle = \int_0^\infty dp p^2 |\psi(p)|^2. \quad (9)$$

The expectation values of the kinetic and potential energy operators are given by

$$\langle \psi | H_0 | \psi \rangle = \int_0^\infty dp p^2 \psi^*(p) p^2 \psi(p), \quad (10)$$

and

$$\langle \psi | V | \psi \rangle = \int_0^\infty dp p^2 \int_0^\infty dp' p'^2 \psi^*(p) V_0(p, p') \psi(p'). \quad (11)$$

III. TWO-BODY BOUND-STATE EQUATION WITHOUT PARTIAL-WAVE DECOMPOSITION

In this approach, the Lippmann–Schwinger equation (2) is projected onto vector momentum states $|\mathbf{p}\rangle$. These states satisfy the completeness relation

$$1 = \int d^3 p |\mathbf{p}\rangle \langle \mathbf{p}|, \quad (12)$$

and are normalized according to

$$\langle \mathbf{p} | \mathbf{p}' \rangle = \delta(\mathbf{p} - \mathbf{p}') = \frac{\delta(p - p')}{p^2} \delta(\hat{\mathbf{p}} - \hat{\mathbf{p}}'). \quad (13)$$

Here $\hat{\mathbf{p}}$ denotes the unit vector specified by the angular variables $\Omega_p = (\theta, \varphi)$. The Dirac delta distribution on the unit sphere is defined by its action

$$\int d\Omega_{\hat{\mathbf{p}}'} \delta(\hat{\mathbf{p}} - \hat{\mathbf{p}}') f(\hat{\mathbf{p}}') = f(\hat{\mathbf{p}}), \quad (14)$$

for any test function $f(\hat{\mathbf{p}})$, where $d\Omega_{\hat{\mathbf{p}}} = d(\cos \theta) d\varphi$. In spherical coordinates (θ, φ) , this distribution can be written explicitly as

$$\delta(\hat{\mathbf{p}} - \hat{\mathbf{p}}') \equiv \delta(\Omega_p - \Omega_{p'}) = \frac{\delta(\theta - \theta')}{\sin \theta} \delta(\varphi - \varphi'). \quad (15)$$

After projection with $\langle \mathbf{p} |$ and insertion of the completeness relation (12), Eq. (2) takes the form

$$\langle \mathbf{p} | \psi \rangle = \int d^3 p' \frac{1}{E - p'^2} \langle \mathbf{p} | V | \mathbf{p}' \rangle \langle \mathbf{p}' | \psi \rangle. \quad (16)$$

We restrict ourselves to interactions for which the matrix element $\langle \mathbf{p} | V | \mathbf{p}' \rangle$ is a rotationally invariant scalar function,

$$\langle \mathbf{p} | V | \mathbf{p}' \rangle = V(\mathbf{p}, \mathbf{p}') = V(p, p', \hat{\mathbf{p}} \cdot \hat{\mathbf{p}}'), \quad (17)$$

where $\hat{\mathbf{p}} \cdot \hat{\mathbf{p}}'$ is the cosine of the angle between \mathbf{p} and \mathbf{p}' .

Introducing the variables $x = \hat{\mathbf{z}} \cdot \hat{\mathbf{p}}$ and $x' = \hat{\mathbf{z}} \cdot \hat{\mathbf{p}}'$, and denoting the azimuthal angles of $\hat{\mathbf{p}}$ and $\hat{\mathbf{p}}'$ by φ and φ' , respectively, Eq. (16) can be written as

$$\begin{aligned} \psi(p, x) = & \int_0^\infty dp' p'^2 \int_{-1}^1 dx' \int_0^{2\pi} d\varphi \frac{1}{E - p'^2} \\ & \times V(p, p', y) \psi(p', x'), \end{aligned} \quad (18)$$

where

$$y = \hat{\mathbf{p}} \cdot \hat{\mathbf{p}}' = x x' + \sqrt{1 - x^2} \sqrt{1 - x'^2} \cos(\varphi - \varphi'). \quad (19)$$

Without loss of generality, the azimuthal angle of $\hat{\mathbf{p}}$ is set to zero.

Defining

$$v(p, p', x, x') \quad (20)$$

$$= \int_0^{2\pi} d\varphi V(p, p', x x' + \sqrt{1 - x^2} \sqrt{1 - x'^2} \cos \varphi),$$

the integral equation reduces to

$$\begin{aligned} \psi(p, x) = & \int_0^\infty dp' p'^2 \int_{-1}^1 dx' \frac{1}{E - p'^2} \\ & \times v(p, p', x, x') \psi(p', x'). \end{aligned} \quad (21)$$

This is a two-dimensional integral equation in the magnitude p and the angular variable x (hereafter referred to as the 2D formulation).

Although Eq. (20) allows the use of the full interaction directly, it is instructive to expand the potential in Legendre polynomials

$$V(p, p', \hat{\mathbf{p}} \cdot \hat{\mathbf{p}}') = \sum_l \frac{2l + 1}{4\pi} P_l(\hat{\mathbf{p}} \cdot \hat{\mathbf{p}}') V_l(p, p'). \quad (22)$$

Inserting this expansion into Eq. (20) yields

$$\begin{aligned} v(p, p', x, x') = & \sum_l \frac{2l + 1}{4\pi} V_l(p, p') \int_0^{2\pi} d\varphi P_l(y) \\ = & \sum_l \frac{2l + 1}{2} V_l(p, p') P_l(x) P_l(x'), \end{aligned} \quad (23)$$

which allows the use of partial-wave-decomposed interactions within the two-dimensional formulation.

To demonstrate the equivalence of the one- and two-dimensional approaches, the wave function is expanded as

$$\psi(p, x) = \sum_l \sqrt{\frac{2l + 1}{4\pi}} \psi_l(p) P_l(x). \quad (24)$$

Substituting Eqs. (24) and (23) into Eq. (21), using the orthogonality of the Legendre polynomials, and integrating over x , one obtains

$$\psi_l(p) = \frac{1}{E - p^2} \int_0^\infty dp' p'^2 V_l(p, p') \psi_l(p'). \quad (25)$$

The two-dimensional equation (21) is therefore equivalent to an infinite set of uncoupled one-dimensional equations, one for each partial wave.

For the interactions considered here, only the $l = 0$ channel is sufficiently attractive to support a bound state. All higher partial waves are suppressed by the centrifugal barrier and do not support negative-energy solutions. As a result, the bound-state solution of the full two-dimensional equation must be a pure s -wave, and its binding energy must coincide with that obtained from the one-dimensional $l = 0$ equation. Verifying this equivalence numerically provides a central validation of the two-dimensional formulation.

The normalization condition reads

$$1 = \langle \psi | \psi \rangle = 2\pi \int_0^\infty dp p^2 \int_{-1}^1 dx |\psi(p, x)|^2, \quad (26)$$

where the factor 2π arises from the analytical integration over the azimuthal angle φ . The expectation values of the kinetic and potential energy operators are given by

$$\langle \psi | H_0 | \psi \rangle = 2\pi \int_0^\infty dp p^2 \int_{-1}^1 dx \psi^*(p, x) p^2 \psi(p, x), \quad (27)$$

and

$$\begin{aligned} \langle \psi | V | \psi \rangle = & 2\pi \int_0^\infty dp p^2 \int_{-1}^1 dx \int_0^\infty dp' p'^2 \int_{-1}^1 dx' \\ & \times \psi^*(p, x) v(p, p', x, x') \psi(p', x') , \end{aligned} \quad (28)$$

where $v(p, p', x, x')$ denotes the potential after the integration over the azimuthal angle φ has been carried out, see Eq. (20).

IV. TWO-BODY BOUND-STATE EQUATION FOR THE YAMAGUCHI POTENTIAL

A. Wave function in momentum space

A rank-one separable potential has the general form

$$V = -|g\rangle 4\pi\lambda \langle g| , \quad (29)$$

where $|g\rangle$ is the form factor and λ is the strength parameter. Inserting Eq. (29) into the Lippmann–Schwinger equation (2) yields, in momentum space,

$$|\psi\rangle = -\frac{1}{E - p^2} |g\rangle 4\pi\lambda \langle g|\psi\rangle = N \frac{1}{\alpha^2 + p^2} |g\rangle , \quad (30)$$

with the scalar quantity

$$N = 4\pi\lambda \langle g|\psi\rangle , \quad \text{and} \quad E = -\alpha^2 . \quad (31)$$

Substituting Eq. (30) into Eq. (31) and assuming $N \neq 0$ yields an implicit relation between λ and the binding energy,

$$\lambda^{-1} = 4\pi \langle g| \frac{1}{\alpha^2 + p^2} |g\rangle . \quad (32)$$

Depending on the explicit form of $|g\rangle$, Eq. (32) can be evaluated analytically. We employ generalized form factors defined for all partial waves,

$$\langle p l | g \rangle \equiv g_l(p) = \frac{p^l}{(p^2 + \beta^2)^{l+1}} . \quad (33)$$

For $l = 0$ this reduces to the original Yamaguchi form factor. A bound state exists only in the $l = 0$ channel for the parameter sets considered here. Inserting $g_0(p)$ into Eq. (32) gives

$$\alpha = \sqrt{\frac{\pi^2 \lambda}{\beta}} - \beta , \quad \text{provided that} \quad \lambda > \frac{\beta^3}{\pi^2} , \quad (34)$$

and the normalized two-body wave function follows from Eqs. (9) and (30),

$$\psi(p) = 2 \sqrt{\frac{\alpha \beta (\alpha + \beta)^3}{\pi}} \frac{1}{\alpha^2 + p^2} \frac{1}{p^2 + \beta^2} . \quad (35)$$

Using Eq. (35), the expectation value of the Hamiltonian can be expressed analytically in terms of α , β , and λ ,

$$\langle \psi | H | \psi \rangle = \langle \psi | H_0 | \psi \rangle + \langle \psi | V | \psi \rangle \quad (36)$$

$$= \left(\alpha \beta \right) + \left(-\frac{\pi^2 \alpha \lambda}{\beta (\alpha + \beta)} \right) = -\alpha^2 . \quad (37)$$

For the error analysis, it is useful to express the exact expectation values as limits of finite momentum cut-offs. We define

$$\langle H_0 \rangle_{\text{cut}} \equiv \int_0^{p_{\text{cut}}} dp p^2 \psi^*(p) p^2 \psi(p) , \quad (38)$$

$$\langle \psi | H_0 | \psi \rangle = \lim_{p_{\text{cut}} \rightarrow \infty} \langle H_0 \rangle_{\text{cut}} , \quad (39)$$

and

$$\langle V \rangle_{\text{cut}} \equiv -4\pi\lambda \left(\int_0^{p_{\text{cut}}} dp p^2 \psi(p) \frac{1}{p^2 + \beta^2} \right)^2 , \quad (40)$$

$$\langle \psi | V | \psi \rangle = \lim_{p_{\text{cut}} \rightarrow \infty} \langle V \rangle_{\text{cut}} . \quad (41)$$

For the Yamaguchi potential with the form factor of Eq. (33), these expressions can be evaluated analytically. The resulting closed forms are given in Appendix A. They provide quantitative upper bounds on the accuracy achievable at finite p_{cut} and guide the choice of mesh resolution.

In the literature, several parameter sets are used for the Yamaguchi potential, often together with different conversion factors. Table I lists the parameter sets considered here, the conversion factors employed, and the exact two-body binding energy E_2 obtained from Eq. (34).

B. Wave function in coordinate space

The coordinate-space wave function is obtained by Fourier transformation of the momentum-space wave function,

$$\psi(r) = \sqrt{\frac{2}{\pi}} \int_0^\infty dp p^2 \psi(p) j_0(pr) , \quad (42)$$

where $j_0(pr) = \sin(pr)/(pr)$ is the spherical Bessel function. For the Yamaguchi form, the integral can be evaluated analytically. Using Eq. (35), one finds

$$\psi(r) = \sqrt{\frac{2 \alpha \beta (\alpha + \beta)}{(\alpha - \beta)^2}} \frac{e^{-\alpha r} - e^{-\beta r}}{r} . \quad (43)$$

This is the normalized $l = 0$ solution of the Schrödinger equation for a separable, non-local interaction in coordi-

TABLE I. Parameters and conversion factors for the Yamaguchi potentials. The resulting two-body binding energies E_2 are calculated using Eq. (34). Listed values are the exact ones used in calculations. Parameter sets YAMA-0, YAMA-21, YAMA-23, and YAMA-96 are defined in this work.

Potential	β [fm $^{-1}$]	λ [fm $^{-3}$]	$(\hbar c)^2/m_N$ [MeV fm 2]	$\hbar c$ [MeV fm]	E_2 [MeV]	Ref.
YAMA-0	1.14525	0.22	41.47106096	197.327053	-2.225936306578	
YAMA-20	1.15	0.22	41.47	197.3286	-2.082301411983	[21]
YAMA-21	1.26102	0.285929	41.47	197.3286	-2.288877666231	
YAMA-23	1.3905818	0.3707654	41.47103997	197.3269804	-2.224567197074	
YAMA-96	1.15	0.184	41.47106096	197.327053	-0.471586629956	
YAMA-I	1.45	0.415	41.47	197.3286	-2.207115916453	[5]
YAMA-II	1.45	0.353	41.47	197.3286	-0.415337462056	[5]
YAMA-III	1.15	0.182	41.47	197.3286	-0.412950588019	[5]
YAMA-IV	1.15	0.179	41.47	197.3286	-0.331781328055	[5]

nate space,

$$-\frac{1}{r^2} \frac{\partial}{\partial r} \left(r^2 \frac{\partial}{\partial r} \psi(r) \right) - 4\pi\lambda g(r) \int_0^\infty dr' r'^2 g(r') \psi(r') = E \psi(r), \quad (44)$$

where the Fourier-transformed interaction reads

$$V(r, r') = -g(r) 4\pi\lambda g(r'), \quad (45)$$

with

$$g(r) = \sqrt{\frac{\pi}{2}} \frac{e^{-\beta r}}{r}. \quad (46)$$

It is convenient to write $\psi(r) = u(r)/r$. Then Eq. (44) becomes

$$-\frac{\partial^2}{\partial r^2} u(r) - 4\pi\lambda g(r) \int_0^\infty dr' r' g(r') u(r') = E u(r), \quad (47)$$

and the normalization condition for $\psi(r)$ reduces to

$$1 = \langle \psi | \psi \rangle = \int_0^\infty dr |u(r)|^2. \quad (48)$$

For any interaction that falls off faster than $1/r^2$ as $r \rightarrow \infty$, the bound-state wave function behaves as

$$\psi(r) \underset{r \rightarrow \infty}{\sim} A_s \frac{e^{-\alpha r}}{r}, \quad (49)$$

where A_s is the asymptotic normalization constant. As $\beta > \alpha$ here, the asymptotic form of Eq. (43) is

$$\psi(r) \underset{r \rightarrow \infty}{\sim} \sqrt{\frac{2\alpha\beta(\alpha+\beta)}{(\alpha-\beta)^2}} \frac{e^{-\alpha r}}{r}. \quad (50)$$

In this case, A_s coincides with the normalization constant in Eq. (43). With the explicit form of Eq. (43), the expectation value of the radius can be evaluated analytically as

$$\langle \psi | \left(\frac{1}{2} r \right) | \psi \rangle = \frac{1}{4} \left(\frac{1}{\alpha} + \frac{1}{\beta} + \frac{2}{\alpha+\beta} \right), \quad (51)$$

and the rms radius is

$$\sqrt{\langle \psi | \left(\frac{1}{2} r \right)^2 | \psi \rangle} = \sqrt{\frac{1}{8} \left(\frac{1}{\alpha^2} + \frac{1}{\beta^2} + \frac{3}{\alpha\beta} + \frac{4}{(\alpha+\beta)^2} \right)}. \quad (52)$$

These exact results can again be written as limits of finite coordinate cut-offs r_{cut} via the expressions in Eqs. (B9) and (B12). They provide upper bounds on the accuracy achievable at finite r_{cut} and guide the choice of mesh resolution.

V. TWO-BODY BOUND-STATE EQUATION FOR THE MALFLIET-TJON POTENTIAL

As a second interaction, we consider local Malfliet-Tjon potentials of Yukawa type [16, 17]. While these potentials do not describe realistic nuclear forces with tensor components and spin-dependence, they possess a strong short-range repulsion (hard core) characteristic of realistic interactions. This feature makes them an ideal testing ground for numerical algorithms, as the strong repulsion generates significant high-momentum components in the wave function, posing a stringent test for the stability of the integral equation solvers and the cut-off convergence. In coordinate space, they are given by

$$V(r) = V_a \frac{e^{-\mu_a r}}{r} + V_r \frac{e^{-\mu_r r}}{r}, \quad (53)$$

where the long-range attractive part is characterized by the strength V_a and the range parameter μ_a . The short-range repulsive part is described by the strength V_r and the range parameter μ_r . For a local potential of this form, the partial-wave matrix elements in momentum space can be obtained from the Fourier transformation

$$V_l(p, p') = \frac{2}{\pi} \int_0^\infty dr r^2 j_l(pr) V(r) j_l(p'r). \quad (54)$$

Inserting Eq. (53) into Eq. (54) yields the closed form

$$V_l(p, p') = \frac{1}{\pi} \left(\frac{V_a}{p p'} Q_l(z_a) + \frac{V_r}{p p'} Q_l(z_r) \right), \quad (55)$$

with

$$z_{a/r} = \frac{p^2 + p'^2 + \mu_{a/r}^2}{2 p p'}, \quad (56)$$

where $Q_l(z)$ denotes the Legendre functions of the second kind for $|z| > 1$. The first few functions are

$$Q_0(z) = \frac{1}{2} \ln \left(\frac{z+1}{z-1} \right), \quad (57)$$

$$Q_1(z) = \frac{z}{2} \ln \left(\frac{z+1}{z-1} \right) - 1, \quad (58)$$

$$Q_2(z) = \frac{1}{4} (3z^2 - 1) \ln \left(\frac{z+1}{z-1} \right) - \frac{3}{2} z. \quad (59)$$

For the numerical treatment, the potential matrix elements are required at the momentum boundaries where p or p' vanishes. There is only a contribution for $l = 0$ in

this limit

$$\begin{aligned} V_0(p, p') \Big|_{p \cdot p' = 0} &= \frac{2}{\pi} \left(\frac{V_a}{p^2 + p'^2 + \mu_a^2} + \frac{V_r}{p^2 + p'^2 + \mu_r^2} \right). \end{aligned} \quad (60)$$

For the formulation without partial-wave decomposition, we require the momentum-space matrix element $\langle \mathbf{p}|V|\mathbf{p}'\rangle$. For a local interaction $\langle \mathbf{r}|V|\mathbf{r}'\rangle = V(r) \delta^{(3)}(\mathbf{r} - \mathbf{r}')$, one has

$$\langle \mathbf{p}|V|\mathbf{p}'\rangle = \frac{1}{(2\pi)^3} \int d^3 r e^{-i(\mathbf{p}-\mathbf{p}') \cdot \mathbf{r}} V(r). \quad (61)$$

Evaluating this integral for Eq. (53) gives

$$\begin{aligned} V(\mathbf{p}, \mathbf{p}') &= \frac{1}{2\pi^2} \left(\frac{V_a}{(\mathbf{p} - \mathbf{p}')^2 + \mu_a^2} + \frac{V_r}{(\mathbf{p} - \mathbf{p}')^2 + \mu_r^2} \right). \end{aligned} \quad (62)$$

With this explicit representation, the azimuthal integral in Eq. (20) can also be evaluated analytically. One finds

$$\begin{aligned} v(p, p', x, x') &= \frac{1}{\pi} \left[\frac{V_a}{\sqrt{(p^2 + p'^2 - 2 p p' x x' + \mu_a^2)^2 - 4 p^2 p'^2 (1 - x^2)(1 - x'^2)}} \right. \\ &\quad \left. + \frac{V_r}{\sqrt{(p^2 + p'^2 - 2 p p' x x' + \mu_r^2)^2 - 4 p^2 p'^2 (1 - x^2)(1 - x'^2)}} \right]. \end{aligned} \quad (63)$$

In the literature, several parameter sets for the Malfliet–Tjon potentials are used, often together with different conversion constants. Table II collects the parameter sets adopted here and the corresponding conversion factors.

VI. NUMERICAL METHODS

The determination of the two-body bound-state energy and wave function in momentum space requires the solution of the homogeneous Lippmann–Schwinger equation (8) or (21) for negative energies. Depending on the interaction, this can be achieved analytically or by transforming the integral equations into matrix eigenvalue problems.

A. Special Case: The Yamaguchi Potential

The separable nature of the Yamaguchi potential allows for more direct methods to find the binding energy than the general matrix eigenvalue approach. First, it can be

calculated exactly using the analytical formula given in Eq. (34). With $E = -\alpha^2$, this equation provides the exact binding energy directly from the potential parameters λ and β .

Alternatively, the binding energy can be found by numerically solving the implicit relation in Eq. (32)

$$\lambda^{-1} = 4\pi \langle g | \frac{1}{E - p^2} | g \rangle = 4\pi \int_0^\infty dp p^2 \frac{g^2(p)}{E - p^2}. \quad (64)$$

To evaluate the integral over the semi-infinite domain, we map the standard Gauss–Legendre interval $x \in (-1, 1)$ to the momentum range $p \in (0, \infty)$ using the transformations

$$p(x) = s \frac{1+x}{1-x} \quad \text{and} \quad dp = \frac{2s}{(1-x)^2} dx, \quad (65)$$

where s is a scaling factor to optimize the point distribution. For the parameter sets considered here, the integrand in Eq. (64) peaks in the momentum range 0.25–0.5 fm⁻¹. Choosing $s = 1$ fm⁻¹ maps the interval

TABLE II. Parameters for the Malfliet–Tjon potentials and conversion factors from the cited references. Listed values are the exact ones used in calculations.

Potential	V_a [MeV fm]	μ_a [fm $^{-1}$]	V_r [MeV fm]	μ_r [fm $^{-1}$]	$(\hbar c)^2/m_N$ [MeV fm 2]	$\hbar c$ [MeV fm]	Ref.
MT-III	−635.306	1.55	1458.047	3.11	41.47	197.3	[16]
MT-IIIa	−626.8932	1.55	1438.7228	3.11	41.47	197.3286	[2]
MT-IV	−65.109	0.633	—	—	41.47	197.3	[1]
MT-IVa	−65.1776	0.633	—	—	41.47	197.3286	[2]
MT-V	−570.3316	1.55	1438.4812	3.11	41.47	197.3	[1]
MT-Vs	−578.089	1.55	1458.047	3.11	41.47	197.3	[22]
MT-VI	−58.7954	0.723	—	—	41.47	197.3	[16]

$x \in (-1, 0)$ to $p \in (0, 1)$, ensuring that the peak region is resolved with high density, while the interval $x \in (0, 1)$ covers the high-momentum tail. The binding energy E_2 is then obtained by solving this equation numerically with a standard root-finding procedure.

B. Discretization of the Integral Equations

For a general potential, the 1D partial-wave-projected Lippmann–Schwinger equation (8) is a homogeneous integral equation. To solve this numerically, we discretize the integral over the continuous variable p' using Gauss–Legendre grid points. For the numerical treatment, the semi-infinite integration domain is truncated at a cut-off momentum p_{cut} . To ensure a sufficient density of quadrature points in the physically important low-momentum region, the integration interval $(0, p_{\text{cut}})$ is subdivided into two parts, $(0, p_0) \cup (p_0, p_{\text{cut}})$, with N_{P1} and N_{P2} points respectively. For the precise distribution of the quadrature points within each sub-interval, we employ the mapping detailed in Ref. [23]. To allow for the evaluation of the wave function at the origin, the point $p = 0$ with weight zero is explicitly added to the mesh. Since both the Green’s function $(E - p^2)^{-1}$ (for $E < 0$) and the potential matrix elements considered here remain finite at $p = 0$, this inclusion does not introduce numerical instabilities. This results in a final momentum mesh of $N_P = N_{P1} + N_{P2} + 1$ points.

For the 1D partial-wave equation (8), this discretization leads to a system of linear equations:

$$\psi(p_i) = \frac{1}{E - p_i^2} \sum_{j=1}^{N_P} [wp_j p_j^2 V_l(p_i, p_j)] \psi(p_j). \quad (66)$$

This represents a matrix eigenvalue problem $\vec{\psi} = K(E) \vec{\psi}$, where the kernel matrix $K(E)$ has dimension $N_P \times N_P$ with elements

$$K_{ij}(E) = \frac{1}{E - p_i^2} wp_j p_j^2 V_l(p_i, p_j), \quad (67)$$

where wp_j are the Gauss–Legendre weights. The method used to determine the solution is described in Sec. VI C.

To solve the 2D Lippmann–Schwinger equation (21), we must discretize two continuous variables. We again use Gauss–Legendre quadrature for both integrations. For the angular variable x , the standard Gauss–Legendre points lie within the open interval $(-1, 1)$. To avoid numerical extrapolation in subsequent applications, we explicitly include the boundary points $x = \pm 1$ in the grid. These auxiliary points are assigned zero weights to preserve the exactness of the quadrature rule. Consequently, the full 2D grid for $\psi(p_i, x_k)$ includes the boundaries $p = 0$ and $x = \pm 1$, ensuring the wave function is defined over the entire closed domain. Applying these quadrature rules to Eq. (21), we obtain

$$\psi(p_i, x_k) = \frac{1}{E - p_i^2} \sum_{j=1}^{N_P} \sum_{l=1}^{N_X} [wp_j p_j^2 wx_l \times v(p_i, p_j, x_k, x_l)] \psi(p_j, x_l). \quad (68)$$

To obtain a standard matrix eigenvalue problem, the two-dimensional wave function $\psi(p_i, x_k)$ is rewritten as a vector of dimension $N = N_P \times N_X$. A composite index $I = (i, k)$ maps each grid point to a single vector index, such that $\psi_I = \psi(p_i, x_k)$. The discretized equation again takes the compact form $\vec{\psi} = K(E) \vec{\psi}$, where the kernel matrix $K(E)$ is of size $N \times N$, and its elements are given by

$$K_{IJ}(E) = \frac{1}{E - p_i^2} [wp_j p_j^2 wx_l v(p_i, p_j, x_k, x_l)], \quad (69)$$

with $I = (i, k)$ and $J = (j, l)$.

C. Solution of the Eigenvalue Problem

Both the 1D and 2D approaches yield a homogeneous equation of the form $\vec{\psi} = \lambda(E) K(E) \vec{\psi}$. The physical binding energy E_2 corresponds to the condition $\lambda(E_2) = 1$. The kernel matrix $K(E)$ is generally non-symmetric and dense. Furthermore, the presence of strong short-range repulsion in potentials like the Malfliet–Tjon interaction leads to large negative eigenvalues in the spectrum of K . Since standard power iteration converges to the eigenvalue with the largest magnitude (often a mode driven by the

repulsive core with a large negative value), it cannot be used directly to find the physical bound state near $\lambda = 1$.

Traditionally, inverse iteration with a shift was employed to isolate the physical state [24, 25]. However, this requires an $O(N^3)$ matrix factorization (such as LU decomposition) at every energy step, which becomes prohibitively expensive for the large matrices encountered in the 2D vector-variable formulation.

In this work, we employ the Restarted Arnoldi Method (RAM) [26], a Krylov subspace technique. Stadler *et al.* [27] pioneered the application of such iterative methods to few-body integral equations to avoid the storage and inversion of large kernel matrices. The algorithm proceeds by constructing an orthogonal basis V_m for the Krylov subspace $\mathcal{K}_m(K, \vec{v}) = \text{span}\{\vec{v}, K\vec{v}, \dots, K^{m-1}\vec{v}\}$ of dimension $m \ll N$. The projection of the large matrix K onto this subspace yields a small $m \times m$ upper Hessenberg matrix $H_m = V_m^T K V_m$. The eigenvalues of H_m , usually obtained via the QR algorithm, provide excellent approximations to the extreme eigenvalues of K .

To ensure convergence to the physical state and minimize memory usage, we use an iterative restarting strategy. If the approximate eigenvector obtained from the subspace of size m (typically $m \approx 40$) does not satisfy the convergence criterion, the method is restarted using this vector as the new initial guess. This process effectively filters out the unphysical components of the spectrum. Since the physical bound state corresponds to the algebraically largest positive eigenvalue of K (distinct from the large negative eigenvalues arising from the repulsive core), the method converges rapidly to the desired solution.

The dominant computational cost in this approach is the matrix-vector multiplication, which scales as $O(N^2)$, in contrast to the $O(N^3)$ scaling of direct inversion methods. This efficiency gain is crucial for the 2D formulation, where N can reach $\mathcal{O}(10^4)$ for dense momentum grids.

VII. RESULTS AND DISCUSSION

A. The Yamaguchi Potential: Benchmarking and Validation

The primary advantage of the Yamaguchi potential is its analytical solvability, which provides an exact benchmark for all numerical methods. In Table I, we list the exact binding energies E_2 for various parameter sets, calculated directly from the analytical expression in Eq. (34). These values serve as the benchmark against which the numerical results are measured.

A first numerical test is to solve the implicit equation (64) for the binding energy. The results for two representative parameter sets, YAMA-23 and YAMA-IV, are shown in Table III. These examples demonstrate that as the number of quadrature points N increases, the calculated binding energy rapidly converges to the exact analytical value. This behavior is typical for all parameter sets investigated. Typically, 32 quadrature points

TABLE III. Convergence of the two-body binding energy E_2 for YAMA-23 and YAMA-IV, obtained by numerically solving the implicit Eq. (64). N denotes the number of Gauss-Legendre integration points.

N	YAMA-23 E_2 [MeV]	YAMA-IV E_2 [MeV]
8	-2.221497086914	-0.333671149537
16	-2.224567143808	-0.331789172180
24	-2.224567197077	-0.331781342438
32	-2.224567197074	-0.331781328071
40	-2.224567197074	-0.331781328055
48	-2.224567197074	-0.331781328055

are sufficient to match the analytical binding energy to 12 significant digits. All potentials reach this level of accuracy by $N = 40$, confirming the high precision of the mapping and quadrature schemes.

Before solving the full integral equation, it is useful to quantify the systematic error introduced by truncating the momentum integration at a finite cut-off p_{cut} . For the Yamaguchi potential, Appendix A provides closed-form expressions for the cut-off dependence of $\langle H_0 \rangle_{\text{cut}}$ and $\langle V \rangle_{\text{cut}}$, and thus for the missing high-momentum contributions. In practice, the same cut-off quantities can be obtained by numerically integrating the analytical wave function, Eq. (35), provided the momentum mesh is sufficiently dense. Throughout this section, we use the convention $\Delta X \equiv X - X_{\text{cut}}$, where X denotes the exact limit $p_{\text{cut}} \rightarrow \infty$.

Table IV summarizes the resulting cut-off dependence for the YAMA-23 potential and also documents the number of Gauss-Legendre mesh points N required to converge the numerical integrals for a given p_{cut} . For example, $p_{\text{cut}} = 50 \text{ fm}^{-1}$ yields an energy error of order 10^{-4} MeV , while $p_{\text{cut}} = 200 \text{ fm}^{-1}$ reduces the error to the 10^{-6} MeV level. The table also illustrates the interplay between cut-off and resolution. While $N = 48$ is sufficient to converge the integrals for $p_{\text{cut}} = 100 \text{ fm}^{-1}$, substantially larger meshes are required when the integration range is extended to very large cut-offs.

The crucial test is the numerical solution of the discretized Lippmann–Schwinger equation (8). Table V shows the expectation values obtained from the eigenvalue calculation over the same set of cut-offs. A direct comparison with Table IV shows that, for each p_{cut} , the converged energy sum $\langle H_0 \rangle_{\text{cut}} + \langle V \rangle_{\text{cut}}$ reproduces the corresponding cut-off benchmark. In particular, the deviation ΔE_2 agrees within the tabulated precision. This indicates that the discretized eigenvalue solution introduces no additional significant numerical error beyond the truncation at p_{cut} .

As a final check, we analyze the bound-state wave function in coordinate space. The coordinate-space wave function $\psi(r)$ is obtained by numerically Fourier transforming the momentum-space solution $\psi(p)$ using Eq. (42). For the Yamaguchi potential this transformation can also be

TABLE IV. Momentum-space convergence for the YAMA-23 potential using the analytical wave function given in Eq. (35). Deviations $\Delta X \equiv X_{\text{exact}} - X_{\text{cut}}$ and $\Delta E \equiv E_2 - (\langle H_0 \rangle_{\text{cut}} + \langle V \rangle_{\text{cut}})$ are relative to the exact limits $\langle H_0 \rangle = 13.35647233$ MeV, $\langle V \rangle = -15.58103952$ MeV, and $E_2 = -2.22456720$ MeV. N is the number of Gauss–Legendre points.

p_{cut} [fm $^{-1}$]	$\langle H_0 \rangle_{\text{cut}}$ [MeV]	$\Delta \langle H_0 \rangle$ [MeV]	$\langle V \rangle_{\text{cut}}$ [MeV]	$\Delta \langle V \rangle$ [MeV]	$\langle H_0 \rangle_{\text{cut}} + \langle V \rangle_{\text{cut}}$ [MeV]	ΔE [MeV]	N
50	13.35627892	$1.93 \cdot 10^{-4}$	-15.58065272	$-3.87 \cdot 10^{-4}$	-2.22437379	$-1.93 \cdot 10^{-4}$	48
100	13.35644813	$2.42 \cdot 10^{-5}$	-15.58099114	$-4.84 \cdot 10^{-5}$	-2.22454300	$-2.42 \cdot 10^{-5}$	48
200	13.35646930	$3.02 \cdot 10^{-6}$	-15.58103347	$-6.05 \cdot 10^{-6}$	-2.22456417	$-3.02 \cdot 10^{-6}$	64
500	13.35647213	$1.94 \cdot 10^{-7}$	-15.58103914	$-3.87 \cdot 10^{-7}$	-2.22456700	$-1.94 \cdot 10^{-7}$	96
1000	13.35647230	$2.49 \cdot 10^{-8}$	-15.58103947	$-4.97 \cdot 10^{-8}$	-2.22456717	$-2.49 \cdot 10^{-8}$	128
2000	13.35647232	$3.20 \cdot 10^{-9}$	-15.58103952	$-6.39 \cdot 10^{-9}$	-2.22456719	$-3.20 \cdot 10^{-9}$	192
3000	13.35647233	$9.15 \cdot 10^{-10}$	-15.58103952	$-1.83 \cdot 10^{-9}$	-2.22456720	$-9.15 \cdot 10^{-10}$	256

TABLE V. Momentum-space convergence for YAMA-23 derived from the numerical solution of the Lippmann–Schwinger Eq. (8). Definitions of Δ -quantities and exact values follow Table IV.

p_{cut} [fm $^{-1}$]	$\langle H_0 \rangle_{\text{cut}}$ [MeV]	$\Delta \langle H_0 \rangle$ [MeV]	$\langle V \rangle_{\text{cut}}$ [MeV]	$\Delta \langle V \rangle$ [MeV]	$\langle H_0 \rangle_{\text{cut}} + \langle V \rangle_{\text{cut}}$ [MeV]	ΔE [MeV]	N
50	13.35569835	$7.74 \cdot 10^{-4}$	-15.58007215	$-9.67 \cdot 10^{-4}$	-2.22437380	$-1.93 \cdot 10^{-4}$	48
100	13.35637551	$9.68 \cdot 10^{-5}$	-15.58091851	$-1.21 \cdot 10^{-4}$	-2.22454300	$-2.42 \cdot 10^{-5}$	48
200	13.35646022	$1.21 \cdot 10^{-5}$	-15.58102439	$-1.51 \cdot 10^{-5}$	-2.22456417	$-3.02 \cdot 10^{-6}$	64
500	13.35647155	$7.77 \cdot 10^{-7}$	-15.58103855	$-9.71 \cdot 10^{-7}$	-2.22456700	$-1.94 \cdot 10^{-7}$	96
1000	13.35647223	$9.68 \cdot 10^{-8}$	-15.58103940	$-1.21 \cdot 10^{-7}$	-2.22456717	$-2.42 \cdot 10^{-8}$	192
2000	13.35647231	$1.21 \cdot 10^{-8}$	-15.58103951	$-1.51 \cdot 10^{-8}$	-2.22456719	$-3.03 \cdot 10^{-9}$	256
3000	13.35647232	$3.96 \cdot 10^{-9}$	-15.58103952	$-4.95 \cdot 10^{-9}$	-2.22456720	$-9.91 \cdot 10^{-10}$	256

carried out analytically, providing an additional exact benchmark. Moreover, Appendix B provides closed-form expressions for the r_{cut} dependence of the relevant expectation values, allowing us to separate truncation effects from discretization errors.

We first validate the coordinate-space quadrature and the sole effect of truncating the integration at r_{cut} by integrating the analytical wave function $\psi(r)$ (Eq. 43) directly. Table VI lists the cut-off expectation values and their deviations from the exact $r_{\text{cut}} \rightarrow \infty$ limits. It shows, for example, that $r_{\text{cut}} \approx 20$ fm is required to reduce the energy error to the 10^{-4} MeV level, while 30 fm reduces it to 10^{-6} MeV. The table also documents the minimum number of Gauss–Legendre points N needed to converge the integrals for each cut-off. This provides a baseline accuracy that a numerical Fourier transformation and subsequent integrations cannot exceed.

Next, we isolate numerical effects originating from the Fourier transformation itself. To this end, we Fourier transform the exact analytical momentum-space wave function $\psi(p)$ from Eq. (35) to coordinate space. The radial Fourier integrals for the reduced wave function $u(r)$ and its derivative $u'(r)$ are evaluated using Simpson quadrature in the dimensionless variable $x = pr$. This ensures that the oscillations of the spherical Bessel functions are resolved with a constant number of grid points per period for any distance r .

For the evaluation of the kinetic-energy expectation value, the operator is rewritten in a form involving only

first derivatives. To avoid numerical differentiation in coordinate space, $u'(r)$ is calculated directly from the Fourier transform by using the analytical derivative of the spherical Bessel function inside the Fourier integral. When applying this to numerical solutions, $\psi(p)$ is interpolated by cubic splines. This method avoids the amplification of interpolation errors and ensures that the coordinate-space expectation values are fully consistent with the momentum-space results.

The coordinate-space observables obtained by transforming the analytical wave function were found to be identical to those derived from the numerical Lippmann–Schwinger solution. This confirms that the observed deviations are dominated by the Fourier transformation and coordinate-space integration rather than the momentum-space discretization. Consequently, we present the results for the full numerical procedure in Table VII. Comparing these results with the analytical baseline established in Table VI reveals that the remaining deviations are consistent with the truncation at r_{cut} . The high precision confirms that the use of the exact Fourier derivative eliminates the numerical noise typically associated with kinetic-energy evaluation in coordinate space.

Complementing the energy analysis, we calculate the mean radius $\langle \frac{1}{2}r \rangle$ and the rms radius $\sqrt{\langle (\frac{1}{2}r)^2 \rangle}$ in coordinate space. To validate these observables, we employ a multi-stage strategy analogous to the energy analysis. First, we establish the exact benchmark values from

TABLE VI. Coordinate-space convergence for YAMA-23 using the analytical wave function given in Eq. (43). Definitions of Δ -quantities follow Table IV. Exact $r_{\text{cut}} \rightarrow \infty$ limits are given in Appendix B.

r_{cut} [fm]	$\langle H_0 \rangle_{\text{cut}}$ [MeV]	$\Delta \langle H_0 \rangle$ [MeV]	$\langle V \rangle_{\text{cut}}$ [MeV]	$\Delta \langle V \rangle$ [MeV]	$\langle H_0 \rangle_{\text{cut}} + \langle V \rangle_{\text{cut}}$ [MeV]	ΔE [MeV]	N
10	13.39283416	$-3.64 \cdot 10^{-2}$	-15.58103278	$-6.74 \cdot 10^{-6}$	-2.18819863	$-3.64 \cdot 10^{-2}$	32
20	13.35682631	$-3.54 \cdot 10^{-4}$	-15.58103952	$-6.09 \cdot 10^{-13}$	-2.22421321	$-3.54 \cdot 10^{-4}$	32
30	13.35647577	$-3.45 \cdot 10^{-6}$	-15.58103952	$-1.78 \cdot 10^{-15}$	-2.22456375	$-3.45 \cdot 10^{-6}$	32
40	13.35647236	$-3.35 \cdot 10^{-8}$	-15.58103952	$-1.78 \cdot 10^{-15}$	-2.22456716	$-3.35 \cdot 10^{-8}$	32
50	13.35647233	$-3.26 \cdot 10^{-10}$	-15.58103952	$-1.78 \cdot 10^{-15}$	-2.22456720	$-3.26 \cdot 10^{-10}$	48
60	13.35647233	$-5.87 \cdot 10^{-12}$	-15.58103952	$5.24 \cdot 10^{-12}$	-2.22456720	$-6.30 \cdot 10^{-13}$	48

TABLE VII. Verification of the numerical Fourier transform for YAMA-23. The numerical solution of the Lippmann–Schwinger Eq. (8) is transformed to coordinate space, and integrals are evaluated on $[0, r_{\text{cut}}]$. Definitions of Δ -quantities and exact values follow Table IV.

r_{cut} [fm]	$\langle H_0 \rangle_{\text{cut}}$ [MeV]	$\Delta \langle H_0 \rangle$ [MeV]	$\langle V \rangle_{\text{cut}}$ [MeV]	$\Delta \langle V \rangle$ [MeV]	$\langle H_0 \rangle_{\text{cut}} + \langle V \rangle_{\text{cut}}$ [MeV]	ΔE [MeV]	N
10	13.39420424	$-3.77 \cdot 10^{-2}$	-15.58103278	$-6.75 \cdot 10^{-6}$	-2.18682854	$-3.77 \cdot 10^{-2}$	32
20	13.35685907	$-3.87 \cdot 10^{-4}$	-15.58103952	$-6.89 \cdot 10^{-9}$	-2.22418045	$-3.87 \cdot 10^{-4}$	32
30	13.35647612	$-3.79 \cdot 10^{-6}$	-15.58103952	$-6.73 \cdot 10^{-9}$	-2.22456340	$-3.80 \cdot 10^{-6}$	32
40	13.35647241	$-8.43 \cdot 10^{-8}$	-15.58103952	$-7.38 \cdot 10^{-9}$	-2.22456711	$-9.17 \cdot 10^{-8}$	48
50	13.35647238	$-5.81 \cdot 10^{-8}$	-15.58103952	$-7.38 \cdot 10^{-9}$	-2.22456713	$-6.55 \cdot 10^{-8}$	48
60	13.35647238	$-4.97 \cdot 10^{-8}$	-15.58103952	$-7.26 \cdot 10^{-9}$	-2.22456714	$-5.70 \cdot 10^{-8}$	48

the analytical $r_{\text{cut}} \rightarrow \infty$ limits derived in Appendix B (Eqs. B9 and B12). Second, we validate the coordinate-space quadrature by numerically integrating the analytical wave function $\psi(r)$, Eq. (43), up to r_{cut} . The results are shown in Table VIII and demonstrate rapid convergence with increasing cut-off.

Next, we compute the radii by Fourier transforming both the analytical and the numerically determined momentum-space wave functions. As with the energies, these two methods yield identical results, confirming the accuracy of the transformation. Table IX shows the radii obtained from the full numerical solution. The values agree with the analytical benchmarks within the expected finite- r_{cut} truncation error. This confirms that the momentum-space solution, the Fourier transformation, and the coordinate-space integrations yield consistent radii.

Finally, Table X demonstrates the numerical equivalence of the one- and two-dimensional formulations for the Yamaguchi potential. Since the interaction acts purely in the s -wave, the binding energies obtained from the 2D equation, both restricted to $l = 0$ and with higher partial waves included up to $l = 12$, match the 1D partial-wave result to at least ten significant digits. This confirms that the vector-variable formulation correctly recovers the partial-wave limit and that the angular integration grid is sufficiently dense. The remaining deviation from the exact analytical value in the tenth decimal place is common to both formulations and arises solely from the discretization of the radial momentum integral.

To further verify the internal consistency of the 2D

approach, we analyzed the angular content of the resulting wave function $\psi(p, x)$. Inverting the expansion in Eq. (24), the partial-wave components are given by

$$\psi_l(p) = \sqrt{\pi(2l+1)} \int_{-1}^1 dx \psi(p, x) P_l(x). \quad (70)$$

Numerical evaluation of this integral confirms that the contributions of higher partial waves ($l > 0$) to the full wave function are suppressed to the level of machine precision ($< 10^{-30}$). This strict preservation of the s -wave character within the full vector formalism confirms the numerical consistency of the implementation.

B. Application to the Malfliet–Tjon Potential

Having validated our numerical framework against the analytically solvable Yamaguchi potential, we now apply it to the local Malfliet–Tjon (MT) interactions. In contrast to the separable Yamaguchi form factors, the MT potentials behave as $1/r$ at short distances. In momentum space this leads to Yukawa-type matrix elements that decay only as $\sim (p^2 + \mu^2)^{-1}$ at large momenta. As a consequence, both the convergence with respect to the momentum cut-off p_{cut} and the required quadrature resolution are expected to be significantly more demanding than for the Yamaguchi benchmarks.

We solve the 1D partial-wave Lippmann–Schwinger equation (8) for the MT parameter sets listed in Table II. The converged binding energies as a function of p_{cut} are

TABLE VIII. Coordinate-space convergence of radius observables for YAMA-23 using the analytical wave function from Eq. (43) for the numerical integration. Δ -quantities are relative to the exact limits from Eqs. (B9)–(B12). The exact values are $\langle \frac{1}{2}r \rangle = 1.56742466$ fm and $\sqrt{\langle (\frac{1}{2}r)^2 \rangle} = 1.93630777$ fm.

r_{cut} [fm]	$\langle \frac{1}{2}r \rangle_{\text{cut}}$ [fm]	$\Delta \langle \frac{1}{2}r \rangle$ [fm]	$\sqrt{\langle (\frac{1}{2}r)^2 \rangle_{\text{cut}}}$ [fm]	$\Delta \sqrt{\langle (\frac{1}{2}r)^2 \rangle}$ [fm]	N
10	1.46804380	$9.94 \cdot 10^{-2}$	1.76806754	$1.68 \cdot 10^{-1}$	32
20	1.56566166	$1.76 \cdot 10^{-3}$	1.93120929	$5.10 \cdot 10^{-3}$	32
30	1.56739976	$2.49 \cdot 10^{-5}$	1.93620389	$1.04 \cdot 10^{-4}$	32
40	1.56742434	$3.18 \cdot 10^{-7}$	1.93630604	$1.73 \cdot 10^{-6}$	32
50	1.56742466	$4.09 \cdot 10^{-9}$	1.93630775	$2.60 \cdot 10^{-8}$	32
60	1.56742466	$2.33 \cdot 10^{-10}$	1.93630777	$2.35 \cdot 10^{-9}$	32

TABLE IX. Coordinate-space convergence of radius observables for the YAMA-23 potential, obtained by Fourier transforming the numerical solution of the Lippmann–Schwinger Eq. (8). Definitions of Δ -quantities and exact values follow Table VIII.

r_{cut} [fm]	$\langle \frac{1}{2}r \rangle_{\text{cut}}$ [fm]	$\Delta \langle \frac{1}{2}r \rangle$ [fm]	$\sqrt{\langle (\frac{1}{2}r)^2 \rangle_{\text{cut}}}$ [fm]	$\Delta \sqrt{\langle (\frac{1}{2}r)^2 \rangle}$ [fm]	N
10	1.46804380	$9.94 \cdot 10^{-2}$	1.76806754	$1.68 \cdot 10^{-1}$	32
20	1.56566166	$1.76 \cdot 10^{-3}$	1.93120929	$5.10 \cdot 10^{-3}$	32
30	1.56739976	$2.49 \cdot 10^{-5}$	1.93620389	$1.04 \cdot 10^{-4}$	32
40	1.56742434	$3.18 \cdot 10^{-7}$	1.93630604	$1.73 \cdot 10^{-6}$	32
50	1.56742466	$3.86 \cdot 10^{-9}$	1.93630775	$2.58 \cdot 10^{-8}$	48
60	1.56742466	$4.68 \cdot 10^{-11}$	1.93630777	$3.01 \cdot 10^{-10}$	48

TABLE X. Two-body binding energies E_2 for the Yamaguchi-type potentials. The exact value is calculated using Eq. (34). 1D refers to the numerical solution of the partial-wave-decomposed Lippmann–Schwinger Eq. (8). 2D refers to the solution of the two-dimensional Lippmann–Schwinger Eq. (21), with the interaction expanded up to $l = 0$ or up to $l = 12$.

Potential	exact E_2 [MeV]	1D E_2 [MeV]	2D ($l = 0$) E_2 [MeV]	2D ($l = 12$) E_2 [MeV]
YAMA-0	-2.225936306578	-2.2259363061	-2.2259363061	-2.2259363061
YAMA-20	-2.082301411983	-2.0823014115	-2.0823014115	-2.0823014115
YAMA-21	-2.288877666231	-2.2888776655	-2.2888776655	-2.2888776655
YAMA-23	-2.224567197074	-2.2245671961	-2.2245671961	-2.2245671961
YAMA-96	-0.471586629956	-0.4715866298	-0.4715866298	-0.4715866298
YAMA-I	-2.207115916453	-2.2071159153	-2.2071159153	-2.2071159153
YAMA-II	-0.415337462056	-0.4153374617	-0.4153374617	-0.4153374617
YAMA-III	-0.412950588019	-0.4129505879	-0.4129505879	-0.4129505879
YAMA-IV	-0.331781328055	-0.3317813279	-0.3317813279	-0.3317813279

TABLE XI. Momentum-space convergence for the MT-III potential derived from the numerical solution of the Lippmann–Schwinger Eq. (8). Expectation values are evaluated on $[0, p_{\text{cut}}]$ using N mesh points. $\Delta E \equiv E_2 - (\langle H_0 \rangle_{\text{cut}} + \langle V \rangle_{\text{cut}})$ quantifies the internal consistency.

p_{cut} [fm $^{-1}$]	$\langle H_0 \rangle_{\text{cut}}$ [MeV]	$\langle V \rangle_{\text{cut}}$ [MeV]	$\langle H_0 \rangle_{\text{cut}} + \langle V \rangle_{\text{cut}}$ [MeV]	E_2 [MeV]	ΔE [MeV]	N
50	11.22961108	-13.63814854	-2.40853746	-2.40853746	$2.75 \cdot 10^{-14}$	128
100	11.22965900	-13.63828308	-2.40862408	-2.40862408	$2.49 \cdot 10^{-14}$	256
500	11.22966464	-13.63829999	-2.40863535	-2.40863535	$7.99 \cdot 10^{-15}$	768
1000	11.22966468	-13.63830010	-2.40863542	-2.40863542	$2.71 \cdot 10^{-14}$	768
1500	11.22966468	-13.63830011	-2.40863543	-2.40863543	$-1.33 \cdot 10^{-14}$	768
2000	11.22966468	-13.63830011	-2.40863543	-2.40863543	$-1.33 \cdot 10^{-14}$	1024

TABLE XII. Same as Table XI, but for the MT-IV potential.

p_{cut} [fm $^{-1}$]	$\langle H_0 \rangle_{\text{cut}}$ [MeV]	$\langle V \rangle_{\text{cut}}$ [MeV]	$\langle H_0 \rangle_{\text{cut}} + \langle V \rangle_{\text{cut}}$ [MeV]	E_2 [MeV]	ΔE [MeV]	N
50	11.79629175	-14.00477146	-2.20847971	-2.20847971	$<1.0 \cdot 10^{-16}$	256
100	11.79706447	-14.00567481	-2.20861034	-2.20861034	$-2.66 \cdot 10^{-15}$	512
500	11.79717521	-14.00580424	-2.20862903	-2.20862903	$-2.13 \cdot 10^{-14}$	768
1000	11.79717599	-14.00580516	-2.20862916	-2.20862916	$-1.64 \cdot 10^{-14}$	1536
1500	11.79717607	-14.00580525	-2.20862918	-2.20862918	$-3.15 \cdot 10^{-14}$	1536
2000	11.79717609	-14.00580527	-2.20862918	-2.20862918	$8.44 \cdot 10^{-15}$	2048
3000	11.79717610	-14.00580529	-2.20862918	-2.20862918	$4.80 \cdot 10^{-14}$	2048
3500	11.79717611	-14.00580529	-2.20862918	-2.20862918	$-4.35 \cdot 10^{-14}$	2048
4000	11.79717611	-14.00580529	-2.20862918	-2.20862918	$-1.15 \cdot 10^{-14}$	2048

TABLE XIII. Coordinate-space convergence for the MT-III potential, derived from the Fourier-transformed numerical solution of the Lippmann–Schwinger Eq. (8). Expectation values are evaluated on $[0, r_{\text{cut}}]$ using N mesh points. ΔE quantifies the consistency with the momentum-space binding energy E_2 .

r_{cut} [fm]	$\langle H_0 \rangle_{\text{cut}}$ [MeV]	$\langle V \rangle_{\text{cut}}$ [MeV]	$\langle H_0 \rangle_{\text{cut}} + \langle V \rangle_{\text{cut}}$ [MeV]	E_2 [MeV]	ΔE [MeV]	N
10	11.26603326	-13.63830007	-2.37226681	-2.40863543	$-3.64 \cdot 10^{-2}$	32
20	11.22997413	-13.63830011	-2.40832597	-2.40863543	$-3.09 \cdot 10^{-4}$	32
30	11.22966715	-13.63830011	-2.40863295	-2.40863543	$-2.48 \cdot 10^{-6}$	32
40	11.22966474	-13.63830011	-2.40863537	-2.40863543	$-6.07 \cdot 10^{-8}$	48
50	11.22966471	-13.63830011	-2.40863540	-2.40863543	$-3.41 \cdot 10^{-8}$	48
60	11.22966471	-13.63830011	-2.40863539	-2.40863543	$-4.02 \cdot 10^{-8}$	48

TABLE XIV. Same as Table XIII, but for the MT-IV potential.

r_{cut} [fm]	$\langle H_0 \rangle_{\text{cut}}$ [MeV]	$\langle V \rangle_{\text{cut}}$ [MeV]	$\langle H_0 \rangle_{\text{cut}} + \langle V \rangle_{\text{cut}}$ [MeV]	E_2 [MeV]	ΔE [MeV]	N
10	11.83909961	-14.00572261	-2.16662300	-2.20862918	$-4.20 \cdot 10^{-2}$	32
20	11.79761395	-14.00580528	-2.20819133	-2.20862918	$-4.38 \cdot 10^{-4}$	32
30	11.79718040	-14.00580528	-2.20862488	-2.20862918	$-4.30 \cdot 10^{-6}$	48
40	11.79717619	-14.00580528	-2.20862909	-2.20862918	$-8.90 \cdot 10^{-8}$	48
50	11.79717616	-14.00580528	-2.20862913	-2.20862918	$-5.60 \cdot 10^{-8}$	48
60	11.79717615	-14.00580528	-2.20862914	-2.20862918	$-4.80 \cdot 10^{-8}$	48

TABLE XV. Coordinate-space convergence of radius observables for the MT-III and MT-IV potentials, obtained by Fourier transforming the numerical solution of the Lippmann–Schwinger Eq. (8). The radius $\langle \frac{1}{2}r \rangle_{\text{cut}}$ and rms radius $\sqrt{\langle (\frac{1}{2}r)^2 \rangle_{\text{cut}}}$ are evaluated on $[0, r_{\text{cut}}]$ using N mesh points.

r_{cut} [fm]	MT-III			MT-IV		
	$\langle \frac{1}{2}r \rangle_{\text{cut}}$ [fm]	$\sqrt{\langle (\frac{1}{2}r)^2 \rangle_{\text{cut}}}$ [fm]	N	$\langle \frac{1}{2}r \rangle_{\text{cut}}$ [fm]	$\sqrt{\langle (\frac{1}{2}r)^2 \rangle_{\text{cut}}}$ [fm]	N
10	1.51978984	1.78605363	32	1.53035364	1.83041195	32
20	1.60626657	1.92902125	32	1.63986398	2.00695201	32
30	1.60754579	1.93269021	32	1.64184639	2.01243497	32
40	1.60756080	1.93275254	32	1.64187490	2.01254894	32
50	1.60756096	1.93275340	32	1.64187527	2.01255088	32
60	1.60756096	1.93275341	48	1.64187528	2.01255091	48
70	1.60756096	1.93275341	48	1.64187528	2.01255091	48

TABLE XVI. Two-body binding energies E_2 for Malfliet–Tjon-type potentials. 1D refers to the numerical solution of the partial-wave-decomposed Lippmann–Schwinger Eq. (8). 2D refers to the solution of the two-dimensional Lippmann–Schwinger Eq. (21), with the potential restricted to $l = 0$, $l = 12$, or without an explicit partial-wave decomposition ($l = \infty$).

Potential	1D E_2 [MeV]	2D ($l = 0$) E_2 [MeV]	2D ($l = 12$) E_2 [MeV]	2D ($l = \infty$) E_2 [MeV]
MT-III	−2.4086354317	−2.4086354317	−2.4086354317	−2.4086354329
MT-IIIa	−2.2310555602	−2.2310555602	−2.2310555602	−2.2310555614
MT-IV	−2.2086291832	−2.2086291832	−2.2086291832	−2.2086291899
MT-IVa	−2.2234114225	−2.2234114225	−2.2234114225	−2.2234114292
MT-V	−0.3500004890	−0.3500004890	−0.3500004890	−0.3500004893
MT-Vs	−0.4139656263	−0.4139656263	−0.4139656263	−0.4139656266
MT-VI	−0.3427329574	−0.3427329574	−0.3427329574	−0.3427329588

summarized in Tables XI and XII. Two observations are central. First, the MT binding energies show a noticeably stronger dependence on p_{cut} than the Yamaguchi results. Whereas YAMA-23 reaches 10^{-6} MeV stability already at $p_{\text{cut}} \simeq 200 \text{ fm}^{-1}$, the MT potentials require cut-offs in the several-hundred to $\mathcal{O}(10^3) \text{ fm}^{-1}$ range before the corresponding changes become negligible at the 10^{-5} – 10^{-7} MeV level. This behavior reflects the harder, local interaction.

Second, the numerical cost is dominated by the mesh resolution required to represent the kernel accurately over the enlarged momentum interval. As seen in Tables XI and XII, increasing p_{cut} necessitates very large numbers of Gauss–Legendre points N to maintain the same level of convergence. Thus, for MT interactions, the cut-off must be chosen together with a sufficiently dense discretization. Otherwise the apparent stability in E_2 can be misleading.

For these non-separable potentials, the coordinate-space wave function is obtained by a numerical Fourier transform of the momentum-space solution. The accuracy of this step is controlled by the same grid parameters. A sufficiently large p_{cut} is required to capture the short-range structure of $\psi(r)$, and a dense low-momentum region is required to reproduce the long-range asymptotic tail. Tables XIII and XIV list the coordinate-space expectation values $\langle H_0 \rangle_{\text{cut}}$ and $\langle V \rangle_{\text{cut}}$ obtained from the transformed wave functions. For both MT-III and MT-IV, the consistency measure $\Delta E \equiv (\langle H_0 \rangle_{\text{cut}} + \langle V \rangle_{\text{cut}}) - E_2$ reaches the 10^{-8} MeV level once $r_{\text{cut}} \gtrsim 40 \text{ fm}$. This demonstrates that the numerical Fourier transformation handles the stiff repulsive core of the MT-IV potential with the same high precision as the soft Yamaguchi interaction. Table XV reports the corresponding radii for MT-III and MT-IV as functions of r_{cut} .

Finally, Table XVI presents a detailed comparison of the binding energies obtained using the 1D and 2D formulations. We consider three cases for the 2D approach: restricting the potential expansion to $l = 0$, including partial waves up to $l = 12$, and using the full vector-variable formulation without partial-wave decomposition ($l = \infty$). The computational efficiency of the iterative Arnoldi solver allowed for the use of very dense momentum grids (up to $N_p = 2048$), which is crucial for these local

potentials. With these dense grids, the results for the 2D ($l = 0$) and 2D ($l = 12$) calculations match the 1D benchmark to the full displayed precision (ten significant digits). The full vector calculation ($l = \infty$) exhibits minute deviations on the order of 10^{-9} MeV (approximately 0.005 eV), which are attributable to the numerical discretization of the angular integral in Eq. (20). As with the Yamaguchi potential, we verified the angular structure of the solution by projecting the full 2D wave function onto Legendre polynomials. The analysis confirms that contributions from $l > 0$ components are suppressed to the level of machine precision ($< 10^{-30}$). This strict preservation of the s -wave character within the full vector formalism confirms the numerical consistency of the implementation. The wave functions in momentum and coordinate space are shown in Fig. 2 and Fig. 3, respectively. Figure 2 clearly illustrates the substantial high-momentum tail generated by the short-range repulsion of the MT potentials compared to the soft Yamaguchi interaction. In coordinate space (Fig. 3), all ground-state wave functions exhibit the expected node-free structure, with the MT potentials showing characteristic suppression at short distances due to the repulsive core.

Taken together, the cut-off convergence patterns and the momentum- and coordinate-space wave functions form a consistent physical picture. Soft, separable interactions lead to rapidly converging observables and smooth wave functions, while local interactions with short-range singularities generate substantial high-momentum components and require significantly larger numerical cut-offs and denser discretization grids. The agreement between analytical benchmarks, momentum-space solutions, and coordinate-space observables shows that the observed convergence behavior is physical rather than numerical in origin.

VIII. SUMMARY AND OUTLOOK

In this work, we solved the two-boson bound-state problem in momentum space using two complementary formulations. We used a traditional one-dimensional partial-wave approach and a two-dimensional approach

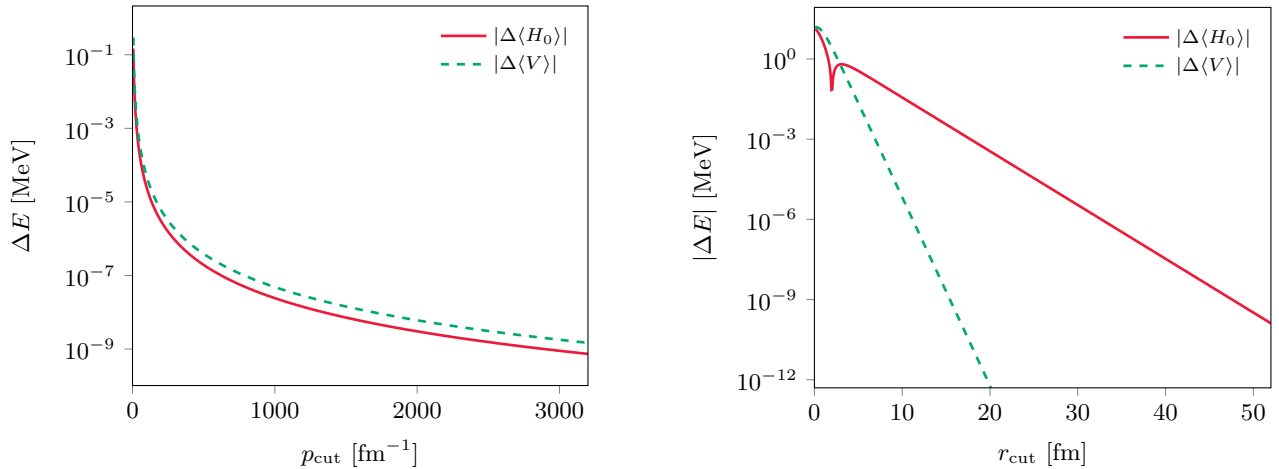


FIG. 1. Convergence of the deviations $\Delta\langle H_0 \rangle$ and $\Delta\langle V \rangle$ from their exact values as functions of the momentum cut-off p_{cut} (left) and the radial cut-off r_{cut} (right) for the YAMA-23 potential.

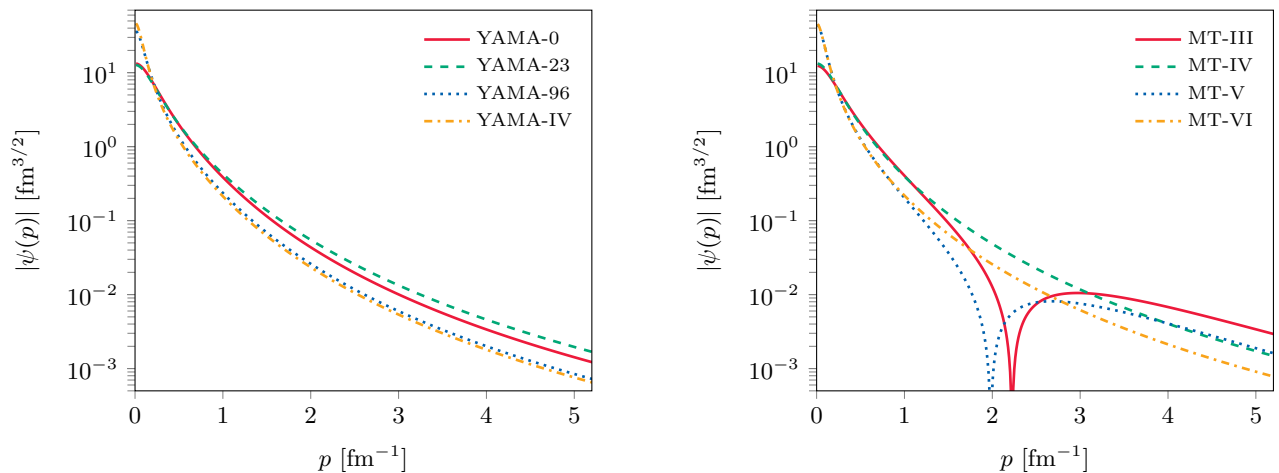


FIG. 2. Momentum-space wave functions $\psi(p)$ for selected Yamaguchi (left) and Malfliet–Tjon (right) potentials, obtained from the solution of the Lippmann–Schwinger equation for $l = 0$.

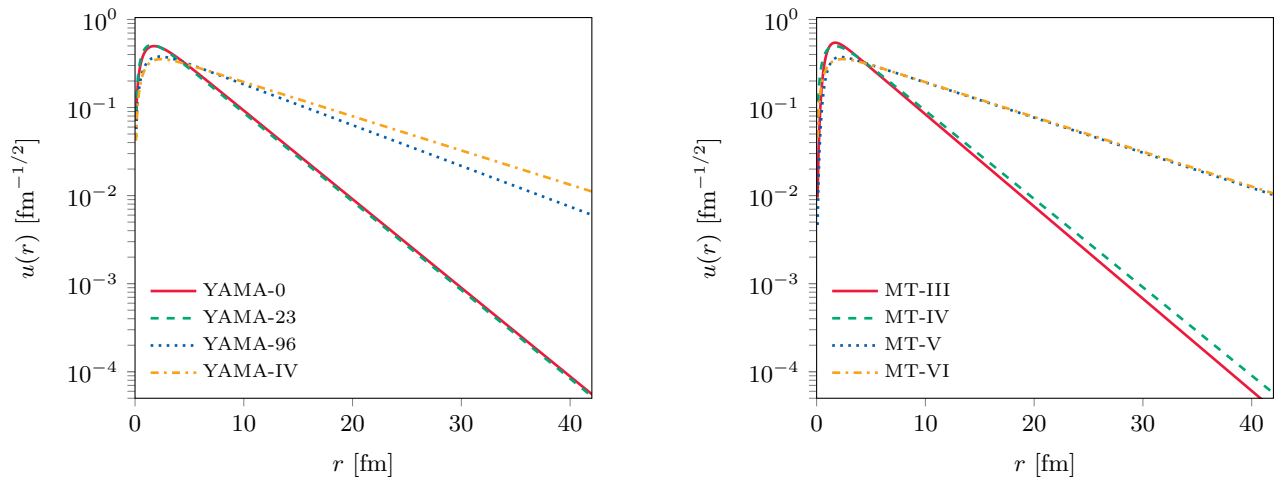


FIG. 3. Reduced coordinate-space wave functions $u(r)$ for selected Yamaguchi (left) and Malfliet–Tjon (right) potentials, obtained by Fourier transformation of the momentum-space solutions.

based on momentum vectors. By applying both methods to the analytically solvable Yamaguchi potential and to the local Malfliet–Tjon interaction, we demonstrated the correctness, stability, and numerical precision of the implementation.

The main achievements of this study are threefold. First, we demonstrated that the 2D vector-variable formulation yields binding energies identical to the 1D partial-wave result to ten decimal places (10^{-10} MeV). This confirms that the vector-variable approach handles the angular integration and the coupling of the momentum grid correctly, a critical validation for future high-energy applications. Second, for the Yamaguchi potential, we derived exact analytical expressions that quantify the systematic errors induced by finite momentum- and coordinate-space cut-offs. Together with the detailed convergence tables, these results provide quantitative benchmarks for estimating numerical uncertainties in momentum-space calculations. Third, the application to the Malfliet–Tjon potentials, including the consistent treatment of higher partial waves in the 2D formulation, demonstrates that

the methods remain reliable for non-separable, local interactions with strong short-range components.

The validated two-body setup presented here provides a building block for more complex few-body calculations. The numerical insights from the cut-off studies and the tested 2D vector-momentum formulation will be used in forthcoming papers on three-body bound-state and scattering problems. The 2D approach closely mirrors the structure of the Faddeev equations and is therefore well suited for extending the present analysis to three-body systems. In this sense, the present study establishes a well-controlled reference for validating the corresponding three-body calculations.

Finally, separable interactions such as the Yamaguchi potential remain a valuable tool in few-body physics. In three-body calculations, they reduce the dimensionality of the Faddeev equations and provide controlled, analytically tractable test cases. This supports the validation of higher-dimensional numerical approaches that employ realistic local potentials. The present work therefore provides a solid basis for future high-precision studies of few-body systems.

Appendix A: Analytical formulas for the Yamaguchi potential in momentum space

To quantify the systematic error introduced by a finite momentum cut-off p_{cut} , we derive exact analytical expressions for the expectation values of H_0 and V as functions of p_{cut} . Using the wave function from Eq. (35), the potential from Eq. (29), and the form factors from Eq. (33) for $l = 0$, the integrals can be calculated analytically. For the kinetic energy we obtain

$$\langle \psi | H_0 | \psi \rangle = \alpha \beta \quad (\text{A1})$$

$$= \lim_{p_{\text{cut}} \rightarrow \infty} \int_0^{p_{\text{cut}}} dp p^2 \psi^*(p) p^2 \psi(p) \quad (\text{A2})$$

$$= \lim_{p_{\text{cut}} \rightarrow \infty} \left[\frac{2 \alpha \beta}{\pi (\alpha - \beta)^3} \left(\frac{(\alpha - \beta)(\alpha + \beta) (2 \alpha^2 \beta^2 + (\alpha^2 + \beta^2) p_{\text{cut}}^2) p_{\text{cut}}}{(p_{\text{cut}}^2 + \alpha^2)(p_{\text{cut}}^2 + \beta^2)} \right. \right. \\ \left. \left. + (\alpha^3 + 3 \alpha \beta^2) \tan^{-1} \left(\frac{p_{\text{cut}}}{\alpha} \right) - \beta (3 \alpha^2 + \beta^2) \tan^{-1} \left(\frac{p_{\text{cut}}}{\beta} \right) \right) \right], \quad (\text{A3})$$

and for the potential energy

$$\langle \psi | V | \psi \rangle = - \frac{\pi^2 \alpha \lambda}{\beta (\alpha + \beta)} \quad (\text{A4})$$

$$= \lim_{p_{\text{cut}} \rightarrow \infty} -4\pi\lambda \left[\int_0^{p_{\text{cut}}} dp p^2 \psi(p) \frac{1}{p^2 + \beta^2} \right]^2 \quad (\text{A5})$$

$$= \lim_{p_{\text{cut}} \rightarrow \infty} \left[- \frac{4 \alpha \lambda}{(\alpha - \beta)^4 \beta (\alpha + \beta) (p_{\text{cut}}^2 + \beta^2)^2} \left(\beta (\beta^2 - \alpha^2) p_{\text{cut}} \right. \right. \\ \left. \left. + (p_{\text{cut}}^2 + \beta^2) \left((\alpha^2 + \beta^2) \tan^{-1} \left(\frac{p_{\text{cut}}}{\beta} \right) - 2 \alpha \beta \tan^{-1} \left(\frac{p_{\text{cut}}}{\alpha} \right) \right) \right)^2 \right]. \quad (\text{A6})$$

The quadratic structure in the last equation reflects the rank-one separable form of the Yamaguchi interaction. Since the momentum-space wave function does not change sign, the cut-off-dependent expressions converge monotonically, as illustrated in Fig. 1.

Appendix B: Analytical formulas for the Yamaguchi potential in coordinate space

We now derive analytical expressions for coordinate-space integrals with a finite radial cut-off r_{cut} , which allow a direct assessment of truncation errors in coordinate space. Using the wave function from Eq. (43), the relevant limits can be evaluated analytically. For the kinetic energy we find

$$\langle \psi | H_0 | \psi \rangle = \alpha \beta \quad (\text{B1})$$

$$= \lim_{r_{\text{cut}} \rightarrow \infty} \int_0^{r_{\text{cut}}} dr r^2 \psi^*(r) \left(-\frac{1}{r^2} \frac{\partial}{\partial r} \left(r^2 \frac{\partial}{\partial r} \right) \right) \psi(r) \quad (\text{B2})$$

$$= \lim_{r_{\text{cut}} \rightarrow \infty} \left[-\frac{\alpha \beta (\alpha + \beta)}{(\alpha - \beta)^2} \left(\alpha + \beta - \alpha e^{-2\alpha r_{\text{cut}}} - \beta e^{-2\beta r_{\text{cut}}} + \frac{2(\alpha^2 + \beta^2)}{\alpha + \beta} (e^{-(\alpha+\beta)r_{\text{cut}}} - 1) \right) \right], \quad (\text{B3})$$

and for the potential energy

$$\langle \psi | V | \psi \rangle = -\frac{\pi^2 \alpha \lambda}{\beta(\alpha + \beta)} \quad (\text{B4})$$

$$= \lim_{r_{\text{cut}} \rightarrow \infty} -4\pi\lambda \left[\int_0^{r_{\text{cut}}} dr r^2 g(r) \psi(r) \right]^2 \quad (\text{B5})$$

$$= \lim_{r_{\text{cut}} \rightarrow \infty} \left[-\frac{4\pi^2 \alpha \beta \lambda (\alpha + \beta)}{(\alpha - \beta)^2} \left(\frac{1 - e^{-(\alpha+\beta)r_{\text{cut}}}}{\alpha + \beta} - \frac{1 - e^{-2\beta r_{\text{cut}}}}{2\beta} \right)^2 \right]. \quad (\text{B6})$$

All cut-off-dependent corrections decay exponentially with r_{cut} , in contrast to the algebraic convergence observed in momentum space. In coordinate space, the Yamaguchi wave function changes sign, leading to partial cancellations in the integrals. For sufficiently large r_{cut} , however, the convergence again becomes monotonic, as shown in Fig. 1.

Closed-form expressions can also be obtained for spatial observables by introducing a cut-off r_{cut} and evaluating the corresponding limits analytically, such as for the mean radius of the two-body system

$$\langle \psi | \left(\frac{1}{2} r \right) | \psi \rangle = \frac{1}{4} \left(\frac{1}{\alpha} + \frac{1}{\beta} + \frac{2}{\alpha + \beta} \right) \quad (\text{B7})$$

$$= \lim_{r_{\text{cut}} \rightarrow \infty} \int_0^{r_{\text{cut}}} dr r^2 \psi^*(r) \left(\frac{1}{2} r \right) \psi(r) \quad (\text{B8})$$

$$= \lim_{r_{\text{cut}} \rightarrow \infty} \left[\frac{\alpha \beta (\alpha + \beta)}{4(\alpha - \beta)^2} \left(\frac{1 - (1 + 2\alpha r_{\text{cut}}) e^{-2\alpha r_{\text{cut}}}}{\alpha^2} + \frac{1 - (1 + 2\beta r_{\text{cut}}) e^{-2\beta r_{\text{cut}}}}{\beta^2} \right. \right. \\ \left. \left. - \frac{8 - 8(1 + (\alpha + \beta)r_{\text{cut}}) e^{-(\alpha+\beta)r_{\text{cut}}}}{(\alpha + \beta)^2} \right) \right], \quad (\text{B9})$$

and the rms radius

$$\sqrt{\langle \psi | \left(\frac{1}{2} r \right)^2 | \psi \rangle} = \sqrt{\frac{1}{8} \left(\frac{1}{\alpha^2} + \frac{1}{\beta^2} + \frac{3}{\alpha \beta} + \frac{4}{(\alpha + \beta)^2} \right)} \quad (B10)$$

$$= \lim_{r_{\text{cut}} \rightarrow \infty} \left[\int_0^{r_{\text{cut}}} dr r^2 \psi^*(r) \left(\frac{1}{2} r \right)^2 \psi(r) \right]^{\frac{1}{2}} \quad (B11)$$

$$= \lim_{r_{\text{cut}} \rightarrow \infty} \left[\frac{\alpha \beta (\alpha + \beta)}{8 (\alpha - \beta)^2} \left(\frac{1}{\alpha^3} - \frac{(1 + 2 \alpha r_{\text{cut}} (1 + \alpha r_{\text{cut}})) e^{-2 \alpha r_{\text{cut}}}}{\alpha^3} \right. \right. \\ \left. \left. + \frac{1}{\beta^3} - \frac{(1 + 2 \beta r_{\text{cut}} (1 + \beta r_{\text{cut}})) e^{-2 \beta r_{\text{cut}}}}{\beta^3} - \frac{16}{(\alpha + \beta)^3} \right. \right. \\ \left. \left. + \frac{8 (2 + (\alpha + \beta) r_{\text{cut}} (2 + (\alpha + \beta) r_{\text{cut}})) e^{-(\alpha + \beta) r_{\text{cut}}}}{(\alpha + \beta)^3} \right) \right]^{\frac{1}{2}}. \quad (B12)$$

[1] Ch. Elster, W. Schadow, A. Nogga, and W. Glöckle, *Few-Body Systems* **27**, 83 (1999).

[2] W. Schadow, Ch. Elster, and W. Glöckle, *Few-Body Systems* **28**, 15 (2000).

[3] H. Liu, Ch. Elster, and W. Glöckle, *Phys. Rev. C* **72**, 054003 (2005).

[4] H. Liu, Ch. Elster, and W. Glöckle, *Nucl. Phys. A* **790**, 262c (2007).

[5] M. R. Hadizadeh and S. Bayegan, *Few-Body Systems* **40**, 171 (2007).

[6] M. R. Hadizadeh and S. Bayegan, *Eur. Phys. J. A* **36**, 201 (2008).

[7] S. Bayegan, M. R. Hadizadeh, and M. Harzchi, *Phys. Rev. C* **77**, 064005 (2008).

[8] M. Harzchi and S. Bayegan, *Eur. Phys. J. A* **46**, 271 (2010).

[9] W. Glöckle, Ch. Elster, J. Golak, R. Skibiński, H. Witała, and H. Kamada, *Few-Body Systems* **47**, 25 (2010).

[10] J. Golak, W. Glöckle, R. Skibiński, H. Witała, D. Rozpedzik, K. Topolnicki, I. Fachruddin, Ch. Elster, and A. Nogga, *Phys. Rev. C* **81**, 034006 (2010).

[11] J. Golak, K. Topolnicki, R. Skibiński, W. Glöckle, H. Kamada, and A. Nogga, *Few-Body Systems* **54**, 2427 (2012).

[12] M. A. Shalchi and S. Bayegan, *Eur. Phys. J. A* **48**, 6 (2012).

[13] M. Harzchi and S. Bayegan, *J. Theor. Appl. Phys.* **8**, 112 (2014).

[14] Y. Yamaguchi, *Phys. Rev.* **95**, 1628 (1954).

[15] Y. Yamaguchi, *Phys. Rev.* **95**, 1635 (1954).

[16] R. A. Malfliet and J. A. Tjon, *Nucl. Phys. A* **127**, 161 (1969).

[17] H. Yukawa, *Proc. Phys.-Math. Soc. (Japan)* **17**, 48 (1935).

[18] M. Mohammadi Sabet, *Acta Phys. Pol. A* **140**, 97 (2021).

[19] M. Hamzavi, M. Movahedi, K.-E. Thylwe, and A. A. Rajabi, *Chin. Phys. Lett.* **29**, 080302 (2012).

[20] M. Napsuciale and S. Rodríguez, *Physics Letters B* **816**, 136218 (2021).

[21] B. F. Gibson and D. R. Lehman, *Phys. Rev. C* **11**, 29 (1975).

[22] N. W. Schellingerhout, *Factorizability in the Numerical Few-Body Problem*, Ph.D. thesis, Rijks Universiteit Groningen (1995).

[23] W. Glöckle, *Computational Nuclear Physics I. Nuclear Structure*, Edited by K. Langanke, J. A. Maruhn, and S. E. Koonin, pp 152 (Springer-Verlag, Berlin-Heidelberg, 1991).

[24] J. H. Wilkinson, *The Algebraic Eigenvalue Problem* (Clarendon Press, Oxford, 1965).

[25] W. Glöckle, *Nucl. Phys. A* **381**, 343 (1982).

[26] W. E. Arnoldi, *Q. Appl. Math.* **9**, 17 (1951).

[27] A. Stadler, W. Glöckle, and P. U. Sauer, *Phys. Rev. C* **44**, 2319 (1991).